The Asian Subtropical Westerly Jet Stream in CRA-40, ERA5, and CFSR Reanalysis Data: Comparative Assessment

Xiaojing YU[1,2], Lixia ZHANG[1,3*], Tianjun ZHOU[1,2,3], and Jingwei LIU[4]

1 *State Key Laboratory of Numerical Modeling for Atmospheric Sciences and Geophysical Fluid Dynamics, Institute of Atmospheric Physics, Chinese Academy of Sciences, Beijing* 100029
2 *University of Chinese Academy of Sciences, Beijing* 100049
3 *CAS Center for Excellence in Tibetan Plateau Earth Sciences, Chinese Academy of Sciences (CAS), Beijing* 100101
4 *National Meteorological Information Center, China Meteorological Administration, Beijing* 100081

(Received June 15, 2020; in final form December 17, 2020)

ABSTRACT

The Asian subtropical westerly jet (AWJ) exerts crucial influences on Eurasian continent weather and climate. This paper analyzes the advantages and limitations of CRA-40, which is China's first generation 40-yr (1979–2018) global atmosphere and land reanalysis product, in describing the characteristics of AWJ, compared with the ECMWF Reanalysis version 5 (ERA5) and NCEP Climate Forecast System Reanalysis (CFSR). The results show a close agreement across the three reanalyses on the whole. (1) In terms of climatology, overall differences of 200-hPa zonal wind across the three reanalyses are within ± 0.5 m s^{-1} (i.e., ± 2%). Large differences with maxima of ± 2 m s^{-1} (± 5%) appear over the Iranian Plateau and south of the Tibetan Plateau in the mid–upper troposphere in winter. (2) For seasonal cycle, the position and intensity of the AWJ centers in the three reanalyses are highly consistent, with correlation coefficient over 0.98. But there are some discrepancies in the zonal shift of the western AWJ center during the transition season. (3) On the interannual timescale, intensity of all AWJ centers varies consistently among the three reanalyses, while larger differences appear in their meridional displacement, especially in the eastern AWJ center. (4) For long-term variations, the three reanalyses all present a significant northward movement of the westerly jet axis in winter, and a southward displacement over central Asia (40°–80°E) and a northward migration over East Asia (80°–110°E) in summer. Thus, this study has provided confidence that CRA-40 has comparable performance with ERA5 and CFSR in depicting the characteristics of AWJ.

Key words: Asian subtropical westerly jet stream (AWJ), reanalysis products, CRA-40

Citation: Yu, X. J., L. X. Zhang, T. J. Zhou, et al., 2021: The Asian subtropical westerly jet stream in CRA-40, ERA5, and CFSR reanalysis data: Comparative assessment. *J. Meteor. Res.*, **35**(1), 46–63, doi: 10.1007/s13351-021-0107-1.

1. Introduction

The Asian subtropical westerly jet stream (AWJ), a narrow and strong westerly belt, exists in the upper troposphere and lower stratosphere over the Eurasian continent all year around. As one of the planetary scale systems at middle latitudes, AWJ is often divided into the eastern part (EAWJ) and the western part (WAWJ) according to their jet center locations and affected area. For instance, AWJ in summer has three active centers located in the Northwest Pacific Ocean, north of the Tibetan Plateau, and the Caspian, respectively, along 40°N (Yang and Zhang, 2008a; Du et al., 2016). EAWJ is closely related to Meiyu (Dao et al., 1958) and the summer monsoon over East Asia (Yeh et al., 1958), while WAWJ is intimately linked with summer precipitation in Northwest China (Yang and Zhang, 2008b; Zhao et al., 2014a) and central Asia (Schiemann et al., 2009; Zhao et al., 2018). Thus, it is of great importance for the AWJ study given its impacts on regional weather and climate.

Meteorological data with high temporal and spatial resolutions have always been in high demand. Unfortu-

Supported by the Program of International S&T Cooperation of Chinese Academy of Sciences (2018YFE0196000) and National Natural Science Foundation of China (41675076).

*Corresponding author: lixiazhang@mail.iap.ac.cn

nately, earlier studies on AWJ were based on inhomogeneous and raw observations at sounding and pilot balloon (pibal) stations. In the 1950s, owing to the rapid development of the aerological network in China, Chinese researchers were able to carry out a series of synoptic and aerological investigations and made remarkable achievements on the general circulation over East Asia (Staff Members of the Section of Synoptic and Dynamic Meteorology, Institute of Geophysics and Meteorology, Academia Sinica, 1957, 1958a, b; Zhu et al., 1990). It is proposed that the seasonal evolution of EAWJ, especially its south–north migration, can be a signal for the seasonal transition of the general circulation, the onset and retreat of the summer monsoon, and occurrence and termination of Meiyu over East Asia (Dao et al., 1958; Yeh et al., 1958; Lu and Schneider, 2017). With the aerological observations increasing, Dao et al. (1965) further illustrated the major features of general circulation over East Asia in the upper troposphere and stratosphere.

With rapid development of numerical weather prediction models, reanalysis products have been prevailing for studying the atmospheric sciences. In the early 21st century, abundant work has been carried out to reveal more refined features of AWJ based on monthly mean variables of modern reanalysis data. For EAWJ, the three-dimensional structures are depicted comprehensively, the seasonal evolution in meridional migration and zonal displacement is reexamined in terms of the intensity and location of its centers and axis, and the thermal mechanism is further investigated by analyzing the meridional difference of air temperature (Kuang et al., 2007). The climate features of AWJ in summer are examined from the perspective of Rossby wave activity (Yang and Zhang, 2008b). In addition, reanalyses data on higher temporal–spatial resolution complement those results based on the monthly mean data. It is noted that the EAWJ core moves westward rapidly during 35th–39th pentads (Zhang et al., 2006) and the median dates of the westerly jet in the Tibetan Plateau point to 28 April and 12 October, by identifying the locations of the jet axis at 6-h intervals (Schiemann et al., 2009).

On interannual and interdecadal timescales, the statistical relationship between AWJ and regional precipitation and associated physical mechanisms have been investigated. In summer, the first two dominant modes of AWJ represent its meridional displacement and southwest–northeast titling (Du et al., 2016). Previous studies demonstrated that the location changes of EAWJ in both meridional and zonal directions have pronounced impacts on the spatial distribution of rainfall anomalies over East Asia through influencing the South Asian high and the western North Pacific subtropical high (Liao et al., 2004; Lin and Lu, 2005; Du et al., 2009; Xie et al., 2015). Moreover, the axis of EAWJ in summer has shifted southward while its intensity in winter enhanced during 1980–2004 relative to 1958–1979 (Zhang and Huang, 2011). In winter, the affected area goes southward along with the retraction of EAWJ (Li and Sun, 2015; Hunt et al., 2018).

It is also proved that the WAWJ has a significant influence on summer rainfall in Northwest China and central Asia (Yang and Zhang, 2008b; Schiemann et al., 2009; Wei et al., 2017; Ji et al., 2020), and the role of its position is more important than its strength (Zhao et al., 2014a, 2018). From the perspective of circulation, the southward displacement of WAWJ is responsible for the rainfall increase in Northwest China, which results in anomalous southerly, water vapor transport, and ascending motion in the lower troposphere (Zhao Y. et al., 2014a, b, 2019; Huang et al., 2015; Peng and Zhou, 2017). Quite a few reasons are attributed to the interannual variation of AWJ position, which is linked with Arctic Oscillation, sea surface temperature anomalies, the Indian summer monsoon, and the South Asian high (Zhao Y. et al., 2014a, 2019; Du et al., 2016; Wei et al., 2017). In the recent decade, reanalysis data are more widely used to evaluate the ability of numerical models in reproducing the fundamental features of AWJ and its relationship with regional precipitation (Huang and Liu, 2011; Yan et al., 2014; Du et al., 2017; Zhao et al., 2018; Lin et al., 2019; Yan et al., 2019; Fu et al., 2020).

Recently, the China Meteorological Administration (CMA) released China's first generation 40-yr (1979–2018) global atmosphere and land reanalysis data (CRA-40; Liu et al., 2017; Zhao B. et al., 2019). It is important for users to know the advantages and limitations of the new reanalysis data. Some researchers have evaluated the performance of the 10-yr (2007–2016) products in terms of global energy cycle, land surface variables, and daily precipitation (Zhao B. et al., 2019; Li et al., 2020; Liang et al., 2020). The objective of this paper is to evaluate the performance of CMA reanalysis in describing AWJ in comparison with the NCEP Climate Forecast System Reanalysis (CFSR) and ECMWF Reanalysis version 5 (ERA5).

The structure of the paper is as follows. Section 2 gives a brief description of the data and method used in this study. Subsequently, comparison results are presented in Section 3, focusing on the climatic structure (Section 3.1), seasonal cycle (Section 3.2), interannual variability (Section 3.3), and long-term change (Section 3.4) of AWJ, respectively. To the end, we conclude with a summary and discussion of our results in Section 4.

2. Data and methods

2.1 *Data*

In this study, we employed three global reanalysis products, CRA-40 from CMA, ERA5 from ECMWF, and CFSR from NCEP. The details of the data are provided as follows.

CRA-40 is the first generation global atmosphere and land reanalysis data produced by CMA. The CMA reanalysis (CRA) project was launched in 2014 (Liu et al., 2017; Zhao B. et al., 2019). The current CRA system is based on the Global System Model (GSM) of the Global Forecast System (GFS) of NCEP and its Gridpoint Statistical Interpolation (GSI) 3DVAR data assimilation system. Compared with other reanalyses, multiple data from conventional observations and satellite instruments, especially over East Asia, have been assimilated into the CRA (Liao et al., 2018; Wang et al., 2018; Yin et al., 2018). CRA-40 has a spacial resolution of 0.312° latitude × 0.312° longitude, with 64 levels in the vertical.

ERA5 is the fifth generation of ECMWF atmospheric reanalysis of the global climate, following FGGE [First GARP (Global Atmospheric Research Program) Global Experiment], ERA-15, ERA-40, and ERA-Interim (Gibson et al., 1997; Uppala et al., 2005; Dee et al., 2011). ERA5 has a horizontal resolution of approximately 31 km and a vertical resolution of 137 levels (Hersbach and Dee, 2016). The ERA data can be obtained at https://www.ecmwf.int/en/forecasts/datasets/reanalysis-datasets/era5.

CFSR is the third generation global reanalysis developed by NCEP, using the Coupled Forecast System (CFS) model (Saha et al., 2010, 2014). CFSR uses a coupled atmosphere–ocean–sea ice–land model, assimilates conventional observations and satellite radiance, and includes the time evolution of CO_2 concentrations. The CFSR data have the same spatial resolution as CRA-40, which are available at https://climatedataguide.ucar.edu/climate-data/climate-forecast-system-reanalysis-cfsr.

In the subsequent comparative assessment, monthly mean variables, including zonal wind, meridional wind, and geopotential height, during the period of 1979–2018 from the three reanalysis datasets are employed. For comparison consistency, all datasets are bilinearly interpolated to a horizontal resolution of 0.5° × 0.5° with 17 vertical levels from 1000 to 100 hPa at an interval of 50 hPa.

2.2 *Methods*

During the boreal summer (JJA) and winter (DJF) seasons, AWJ is located at its preferred positions, and the boreal spring (MAM) and autumn (SON) seasons are the transition periods. Thus, we mainly concentrate on comparison of results in JJA and DJF seasons.

Various verification statistics including pattern correlation coefficient, Pearson linear correlation coefficient, root mean square difference (RMSD), and relative difference, are applied to assess the performance of the three reanalysis datasets. Standard deviation reveals the variation or dispersion from the average, and the interannual standard deviation (ISD) denotes interannual variations relative to the climatic mean (Huang et al., 2014). In addition, the Empirical Orthogonal Function (EOF) analysis method is used to calculate indices and long-term trends of AWJ (Du et al., 2016; Zhao et al., 2014a, 2018).

3. Results

3.1 *Climatic three-dimensional structure of AWJ*

We first assess the differences among the three reanalysis datasets in capturing the climatic horizontal distribution of AWJ (Fig. 1) and the associated circulations (Fig. 2). Figures 1a and b (Figs. 2a, b) depict the climatology of the zonal wind (circulations) at 200 hPa in winter and summer during 1979–2018 from CRA-40. In winter, the jet stream is strong and wide, quasi-zonally orientated within 20°–50°N (Fig. 1a), and the westerlies prevail over Eurasia because of the meridional temperature gradient caused by warm tropics and cold Eurasian continent (Fig. 2a). Two centers appear over western Asia (30°–50°E), and the eastern Asia and western Pacific (110°–160°E) region, respectively. The eastern center (with a maximum wind speed above 70 m s^{-1}) is much stronger and larger than the western one (with the maximum wind speed above 50 m s^{-1}). The horizontal structures of AWJ in spring and autumn are generally similar to that in winter, except that the jet stream is located slightly northward and the jet centers are weaker (figures omitted). In summer, the horizontal structure of the 200-hPa zonal wind differs remarkably from that in other seasons. The jet stream migrates northward and becomes narrow, occupying over 30°–45°N, and the intensity of the zonal wind is strikingly weakened to 25 m s^{-1} (Fig. 1b). This is resulted from the summer South Asian high, which is an intense anticyclonic system located over the Iranian and Tibetan plateaus (Fig. 2b). There exhibit three active jet cores located over the Caspian (50°E), north of the Tibetan Plateau (80°–100°E), and the Northwest Pacific Ocean (140°–160°E), respectively, among which the central one is the strongest with a maximum speed above 30 m s^{-1}.

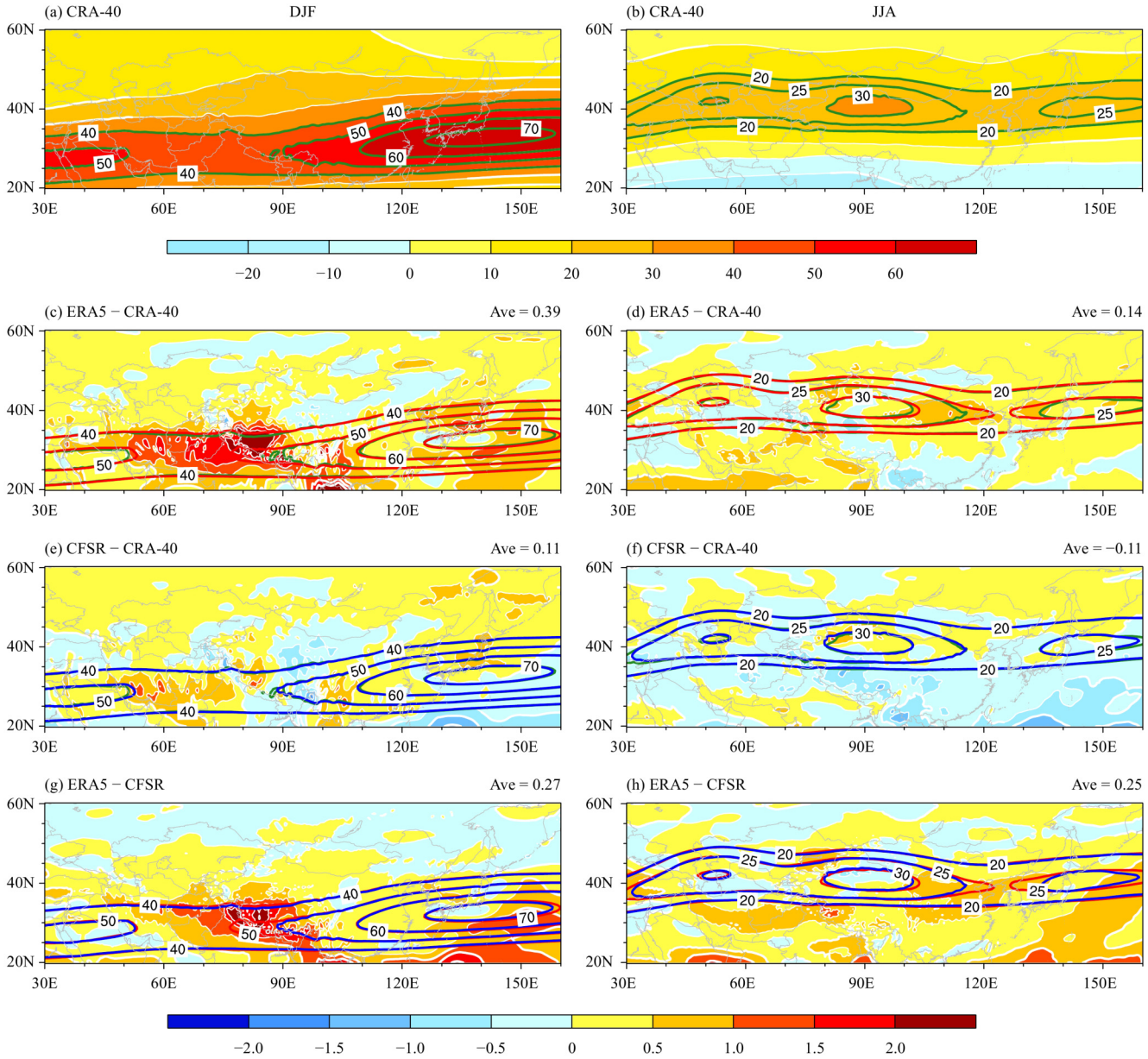

Fig. 1. Climatology of 200-hPa zonal wind (contour; m s^{-1}) from (a, b) CRA-40 and (c–h) the differences (shaded; m s^{-1}) between the three reanalyses in boreal winter (left panels; DJF) and summer (right panels; JJA) averaged over 1979–2018. The contours denote zonal wind speed larger than 40 m s^{-1} (20 m s^{-1}) in winter (summer) from CRA-40 (green), ERA5 (red), and CFSR (blue), respectively. (c, d) ERA5 minus CRA-40, (e, f) CFSR minus CRA-40, and (g, h) ERA5 minus CFSR. The number in the right corner of each plot is the area mean difference between two reanalyses.

The climatic horizontal structures of AWJ from ERA5 and CFSR show comparable spatial patterns and intensity to CRA-40 (figures omitted), with their pattern correlation coefficients excelling 0.99 and regional average differences below 0.4 m s^{-1}. To reveal the detailed differences of the three reanalyses, the differences of the zonal wind and circulations at 200 hPa in winter and summer between each pair are then calculated as shown in Figs. 1c–h; 2c–h. In general, the differences are slightly larger in winter than in summer, although their averages are quite small. In winter, CRA-40 and CFSR exhibit high consistency, with their zonal wind (geopotential height) differences in the range of ± 0.5 m s^{-1} (± 8 gpm) over almost the whole region (Figs. 1e, 2e), whereas ERA5 shows larger inconsistency compared with them (Figs. 1c, g; 2c, g). One region with zonal wind difference exceeding 2 m s^{-1} is located over the Iranian Plateau and the south of the Tibetan Plateau (50°–90°E) between the two jet cores, accompanied by positive geopotential height differences and anticyclonic circulation anomalies.

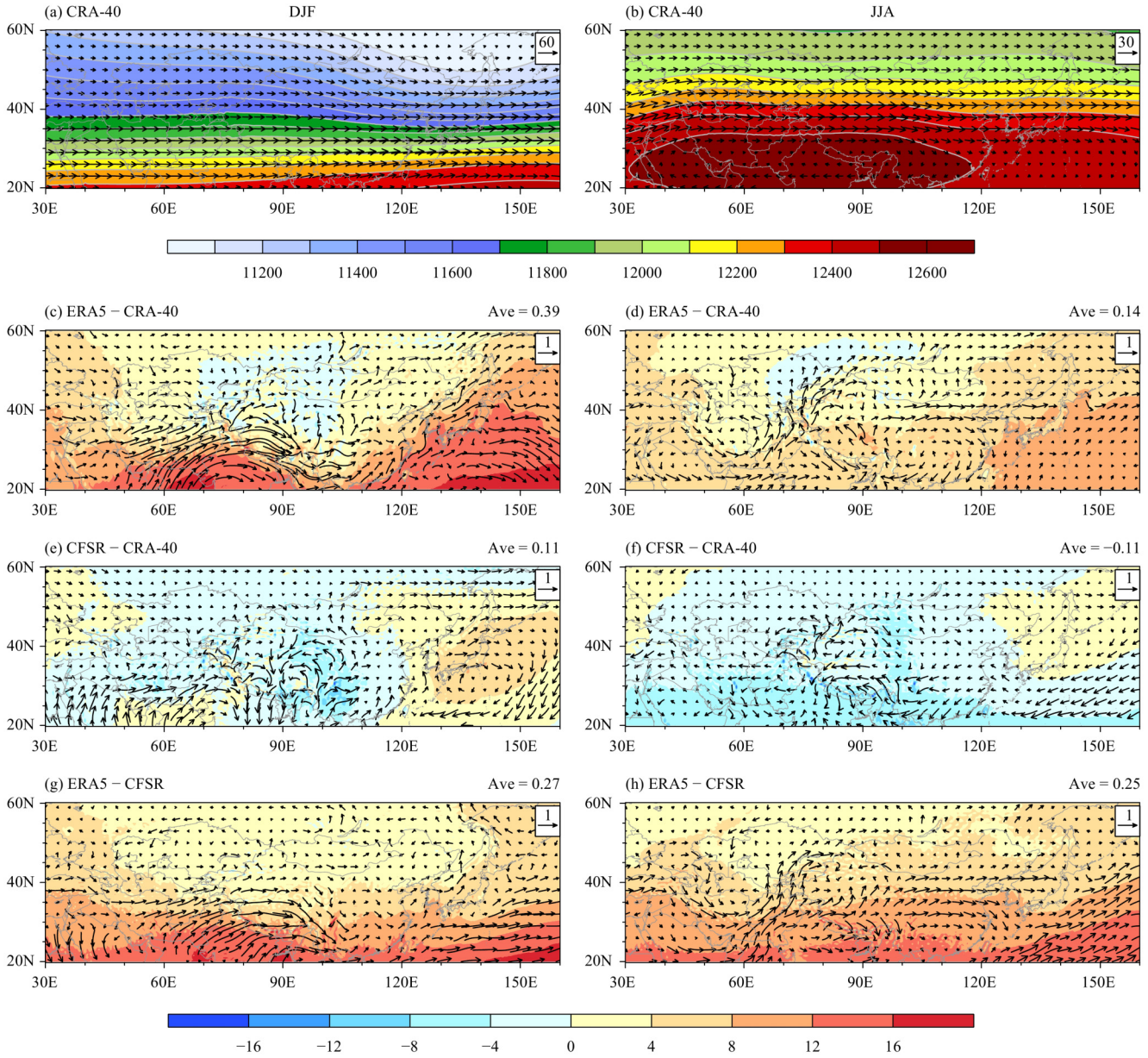

Fig. 2. As in Fig. 1, but for the climatology of geopotential height (shade; gpm) and wind (vector; m s^{-1}) at 200 hPa.

The other region with obvious differences in zonal wind and circulations is situated in western Pacific, southeast of the stronger jet core. In summer (Figs. 1c, e, g; 2c, e, g), differences in zonal wind (geopotential height) between the three reanalyses range within ± 0.5 m s^{-1} (± 8 gpm) over a majority of regions, along with weaker circulation anomalies.

We then evaluate the performance of the three reanalyses in capturing the vertical structures of climate mean AWJ, as illustrated in Fig. 3. Figures 3a and b show the vertical structures of the zonal wind averaged over 30°–160°E in winter and summer from CRA-40. In winter, the whole atmosphere is almost dominated by the westerly. The jet center is at 200 hPa around 30°N with the maximum wind speed of about 50 m s^{-1}. In summer, the jet center migrates northward to around 42°N and the intensity weakens to approximately 20 m s^{-1}. Meanwhile, the tropical region is occupied by a tilted structure, with relatively strong easterly in the middle and upper troposphere and weak westerly in the lower troposphere.

The vertical structures of AWJ from ERA5 and CFSR resemble CRA-40 with their pattern correlation coefficients exceeding 0.99 (figures omitted). Figures 3c–h further give the vertical structure differences in zonal wind across the three reanalyses. Overall, the results agree with that of horizontal distribution of AWJ (Fig. 1). The

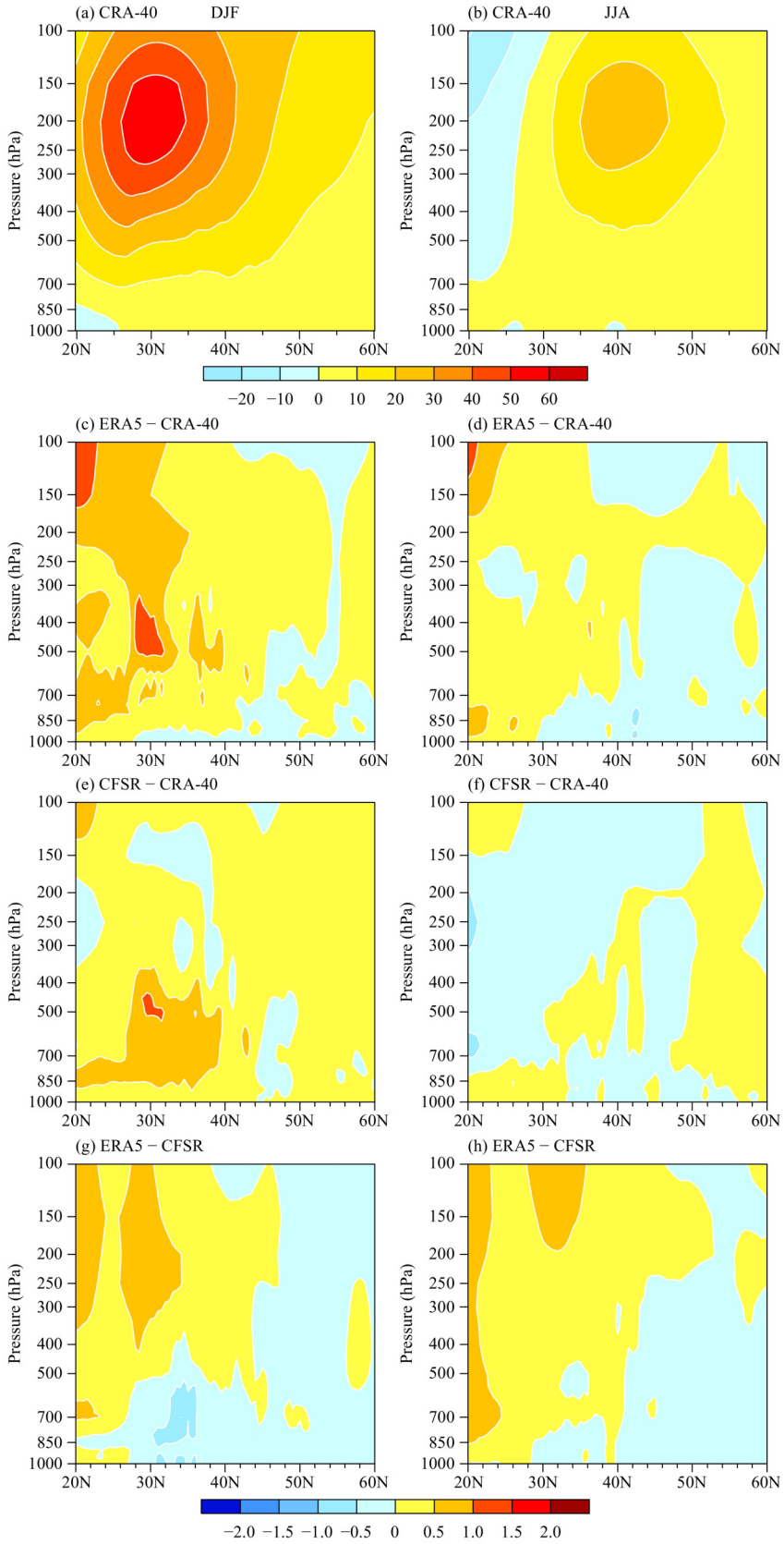

Fig. 3. Latitude–height distributions of zonal wind (m s^{-1}) averaged along 30°–160°E from (a, b) CRA-40 and (c–h) the differences between the three analyses in DJF (left panels) and JJA (right panels) averaged over 1979–2018. (c, d) ERA5 minus CRA-40, (e, f) CFSR minus CRA-40, and (g, h) ERA5 minus CFSR.

differences in summer change within the range of ± 0.5 m s^{-1} (Figs. 3c, e, g), weaker than that in winter (Figs. 3d, f, h). In winter, the difference with a maximum > 0.5 m s^{-1} occupies the south of 40°N, consistent with its horizontal distribution at 200 hPa. It is obvious that the most significant difference between ERA5 and CRA-40 appears in the middle and upper troposphere (above 500 hPa), with the maximum wind speed over 1.5 m s^{-1} (Fig. 3c). CFSR and CRA-40 differ mainly in the lower troposphere (400–850 hPa), with the maximum wind of approximately 1 m s^{-1} (Fig. 3e). The inconsistency between ERA5 and CFSR appears at middle and upper levels (above 400 hPa), with the difference values below 1 m s^{-1} (Fig. 3g).

From the above analysis, we can see that there exhibit some discrepancies among the three reanalyses, especially over the Iranian Plateau and the south of the Tibetan Plateau (around 30°N) in the middle and upper troposphere. Considering that their overall relative differences range within 2% (figures omitted), the three reanalyses also have a high consistency in depicting the three-dimensional structures of AWJ.

3.2 *Seasonal cycle of AWJ*

To further compare the performance of CRA-40, ERA5, and CFSR in depicting the seasonal cycle of AWJ, we select latitude, longitude, and intensity (measured by zonal wind speed) of the jet centers as the metrics. Given there are two main AWJ centers in each month (figures omitted), we divide AWJ into two parts: the western section (30°–70°E) and the eastern section (70°–160°E). Figure 4 illustrates the seasonal cycle of AWJ centers in terms of longitude, latitude, and intensity derived from CRA-40, ERA5, and CFSR. AWJ centers identified from the three reanalyses all undergo a pronounced seasonal cycle. The south–north displace-

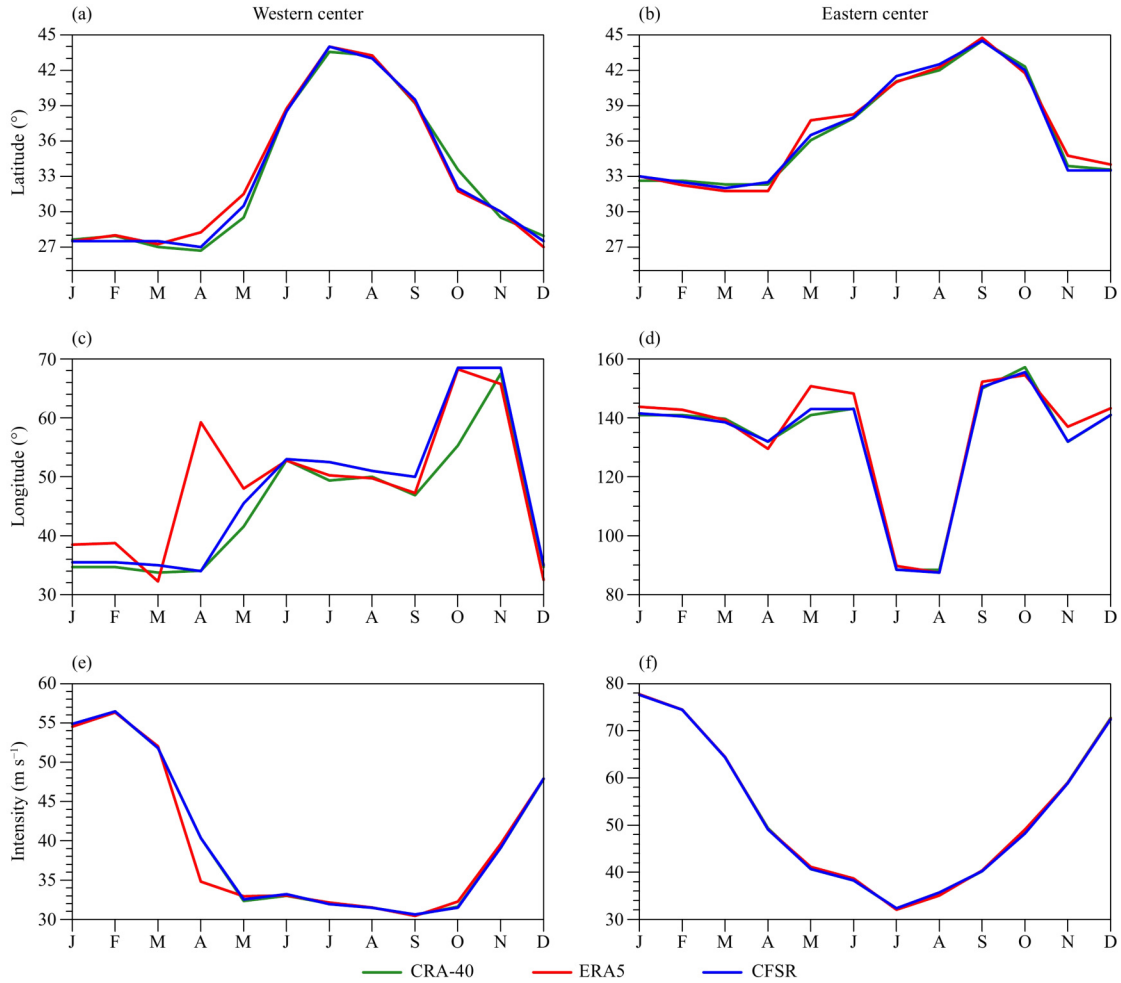

Fig. 4. Seasonal cycle of the (a, c, e) western and (b, d, f) eastern centers of AWJ in terms of (a, b) latitude, (c, d) longitude, and (e, f) intensity, identified from CRA-40 (green line), ERA5 (red line), and CFSR (blue line). The western and eastern centers are identified over the region of (30°–70°E, 70°–160°E), respectively.

ments of the jet centers are within 10 latitudes, whereas the east–west shifts are more than 50 longitudes.

As for the western center (Figs. 4a, c, e), it stays at about (27°N, 35°E) from January to March, with the maximum zonal wind speed of about 55 m s^{-1}. During its northward migration from April to July, the center reaches the northernmost position at 44°N in July, moves eastward to near 50°E, and weakens abruptly to about 32 m s^{-1}. Subsequently (August–November), the center withdraws southward and intensifies gradually, while continues to move eastward and reaches the easternmost position at near 69°E. In December, the center recedes to its southernmost and westernmost position at about (27°N, 35°E), with the zonal wind speed of 48 m s^{-1}.

The seasonal cycle of the eastern center (Figs. 4b, d, f) exhibits slightly different characteristics, compared with the western one. From January to March, the center is located at about (32°N, 140°E), 5 degrees north compared to the western center, with its intensity decreasing from the maximum of 77 m s^{-1} in January. During the northward migration from April to August, the eastern center settles in its northernmost location of near 45°N in August, one month later than the western one, while the minimum zonal wind speed of 32 m s^{-1} appears in July. Meanwhile, the center migrates zonally by a large margin, reaching its westernmost position of 90°E nearby in August. After that (from September to December), the center recedes quickly to its wintertime position (32°N, 140°E), with the zonal wind intensified.

On the whole, the three reanalyses are highly consistent, with most correlation coefficients higher than 0.98 (Table 1), in describing the seasonal cycle characteristics of AWJ. It is worth noting that there are still some recognizable discrepancies between them, especially during the transition period. For the western center, in spring, the AWJ position derived from ERA5 is further north and east than CRA-40 and CFSR, while its intensity is weaker than CRA-40 and CFSR. In autumn, the AWJ center in CRA-40 recedes southward slowly while moves eastward earlier than in the other two reanalyses. The correlation coefficient between ERA5 and CRA-40 (CFSR) is only 0.76 (0.80). As for the eastern center, the differences are much smaller. In spring and winter, the AWJ center in ERA5 sways at a slightly larger range in the latitude and longitude than CRA-40 and CFSR. Therefore, we need to pay attention to the disagreement in the three reanalyses when examining the zonal shift of AWJ, especially the western center.

3.3 *Interannual variability of AWJ*

We further compare the ability of the three reanalyses in depicting the interannual variation of AWJ, which is represented by ISD (figures omitted). In general, ISD is higher, with a wider coverage, in winter than in summer, similar to the distribution of AWJ. Although there are large differences in the amplitude and pattern of ISD between winter and summer, ISD centers reside at the entrance and exit regions along the AWJ axis, which accords with the previous study by Du et al. (2016). In terms of the differences of ISD among the three reanalyses, relatively high values are located along the jet axis, and the differences in winter are still slightly higher than in summer.

As shown in Figs. 1a, b, there are two AWJ centers in winter, denoted as W1 (western) and W2 (eastern), respectively, and three in summer, denoted as S1 (western), S2 (central), and S3 (eastern), respectively. We then examine the interannual variability of the five centers across the three reanalyses, respectively, with respect to latitude, longitude, and intensity (Fig. 5). Every center exhibits obvious interannual variability during the past 40 years, and the consistency across the three reanalyses is generally higher in summer (S1, S2, and S3) than in winter (W1 and W2). For the meridional migration (Figs. 5a–e), the three reanalyses present considerable agreement with each other, with correlation coefficient $\geqslant 0.88$ and RMSD $\leqslant 0.35$ latitudes. As to the zonal displacement (Figs. 5f–j), the differences for four centers (W1, W2, S1, and S2) across the three reanalyses tend to be larger, especially in the recent decade. The correlation coefficients are relatively lower and most RMSDs are approximately 1.0 longitude, some even exceeding 2.0 longitudes. Taking S2 as an example (Fig. 5i), which is located to the north of the Tibetan Plateau, the correlation coefficient between CRA-40 and ERA5 (between ERA5 and CFSR) is only 0.73 (0.79) while the RMSD is 2.02

Table 1. Pearson correlation coefficients (values < 0.8 are in bold) of the seasonal cycle of AWJ identified from CRA-40, ERA5, and CFSR

		CRA-40 & ERA5	CRA-40 & CFSR	ERA5 & CFSR
Western center	latitude	0.988	0.990	0.997
	longitude	**0.758**	0.962	**0.798**
	Intensity	0.986	0.999	0.986
Eastern center	latitude	0.989	0.998	0.990
	longitude	0.988	0.999	0.993
	Intensity	0.999	0.999	0.999

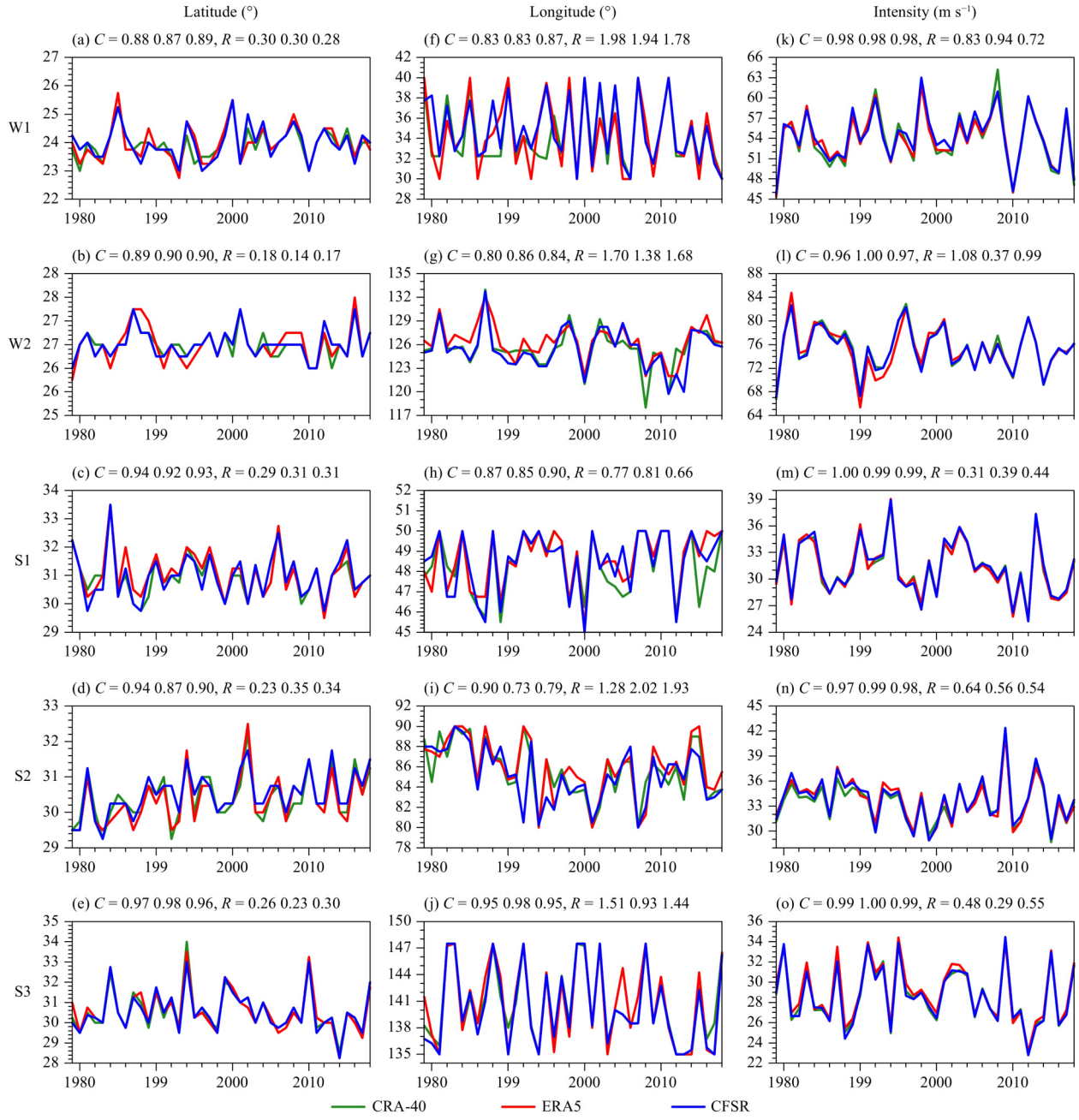

Fig. 5. Time series of AWJ centers in terms of (a–e; °) latitude, (f–j; °) longitude, and (k–o; m s^{-1}) intensity in winter (W1 and W2) and summer (S1, S2, and S3) during 1979–2018, identified from CRA-40 (green line), ERA5 (red line), and CFSR (blue line). Numbers after *C* (*R*) denote the Pearson correlation coefficient (RMSD) between CRA-40 and ERA5, CRA-40 and CFSR, and ERA5 and CFSR in sequence. W1 and W2 indicate the jet centers over the western Asia (30°–50°E) and eastern Asia and western Pacific (110°–160°E) in winter; while S1, S2, and S3 denote the jet centers over the Caspian (50°E), north of the Tibet Plateau (80°–100°E), and the Northwest Pacific Ocean (140°–160°E) in summer, respectively, as shown in Figs. 1a, b.

(1.93) longitudes. Of the three metrics, the intensity for each center from the three reanalyses shows almost complete agreement, with the correlation coefficient approximating 1.0 and RMSD ⩽ 1.0 m s^{-1} (Figs. 5k–o).

We further quantitatively assess the performance of the three reanalyses in reproducing the interannual variability of AWJ centers in each month. Here, we still divide AWJ into the western and eastern sections in calculation, as in Section 3.2. The statistical results including Pearson correlation coefficient, RMSD, and average difference are summarized in Fig. 6. On the whole, the three reanalyses agree more to each other for the western center than the eastern one, with relatively higher correlation coefficients, lower RMSDs, and lower average dif-

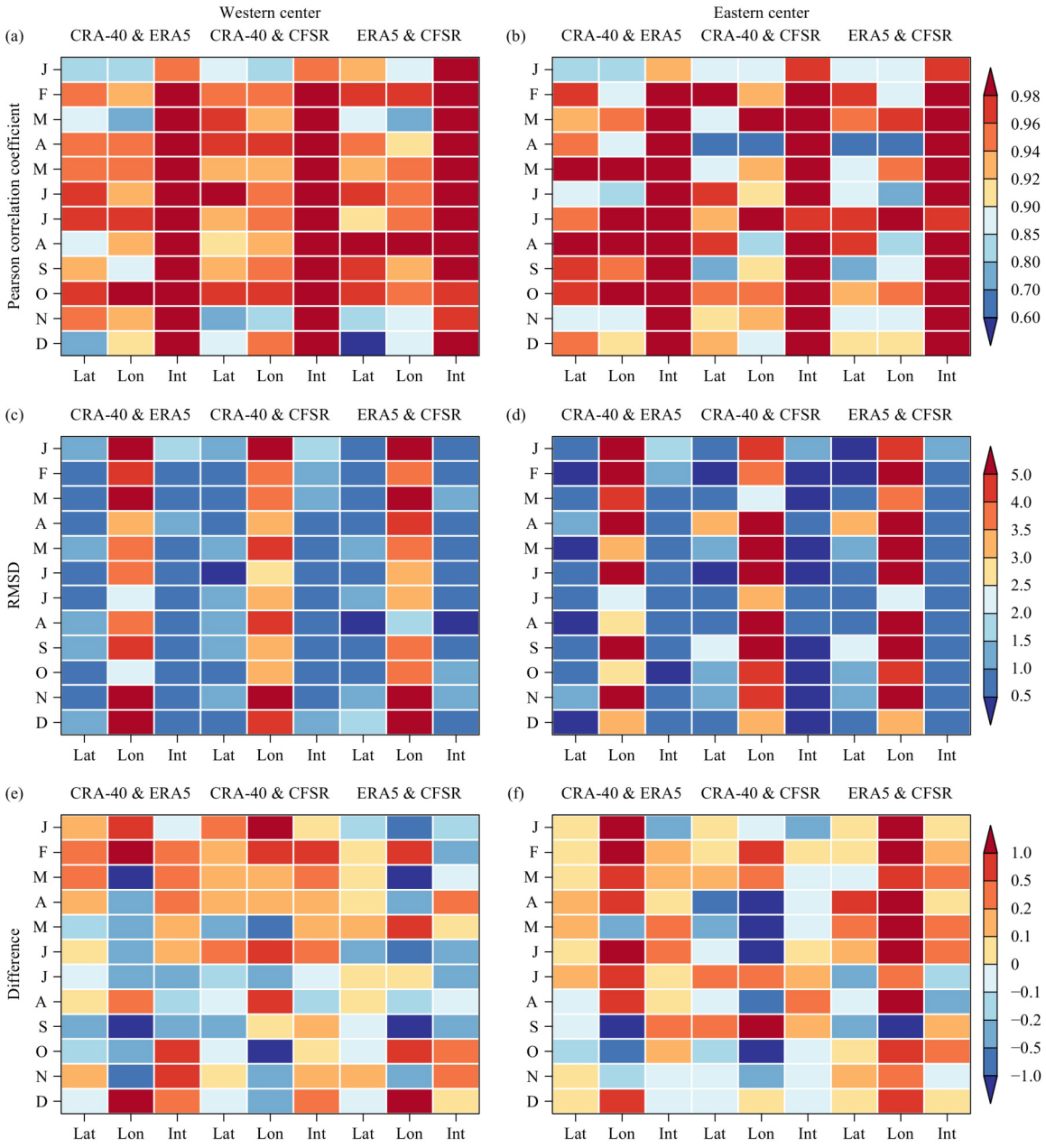

Fig. 6. Statistical results for monthly mean latitude (Lat), longitude (Lon), and intensity (Int) of the (a, c, e) western and (b, d, f) eastern centers of AWJ, respectively, derived from CRA-40, ERA5, and CFSR. The western and eastern centers are identified as in Fig. 3. (a, b) Pearson correlation coefficients, (c, d) root mean square difference (RMSD), and (e, f) average difference.

ferences. Of the three metrics, the three reanalyses have the highest consistency in the intensity while the largest difference in the zonal displacement of AWJ centers. For intensity in each month, the correlation coefficients all exceed 0.94, the RMSDs are below 2.0 m s^{-1}, and the average differences are almost within ± 0.5 m s^{-1}. As to the latitude, the correlation coefficients are within 0.8–0.94, while most RMSDs are below 2.0 latitudes. As regard to the longitude, the correlation coefficients are more scattered (0.7–0.98), and the RMSDs (average differences) exceed 3 (± 0.5) longitudes, especially for the eastern center.

Previous studies have demonstrated that the first two leading EOF modes (EOF1 and EOF2) of 200-hPa zonal wind in summer reflect the changes in position and strength of the subtropical westerly jet over a certain region, thus the corresponding principal components, PC1 and PC2, have often been defined as the position and strength indices, respectively, to investigate the impacts of the subtropical westerly jet to weather and climate (Zhao et al., 2014a, 2018; Du et al., 2016; Yan et al., 2019). Similarly, by applying the EOF decomposition to

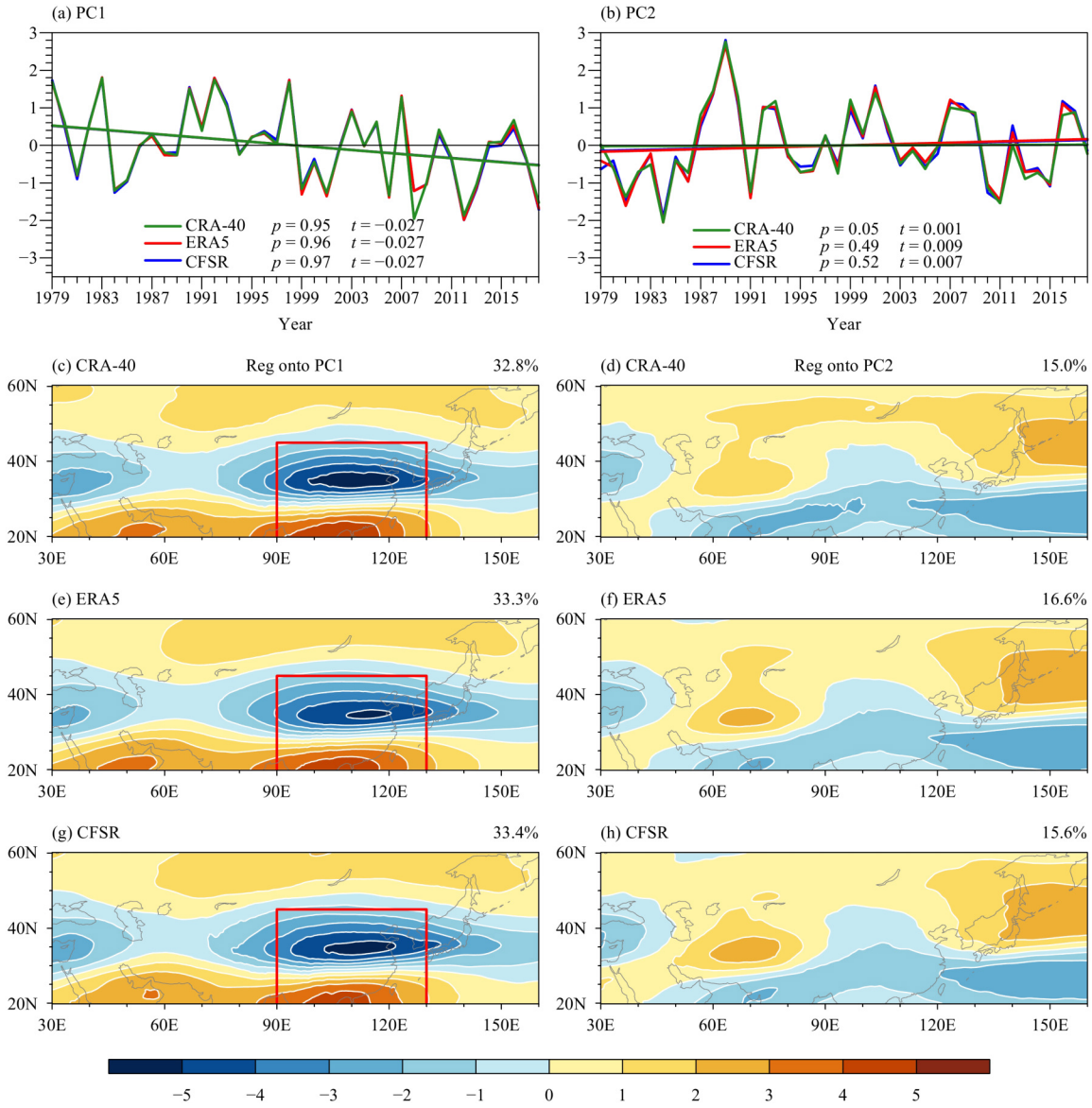

Fig. 7. (a, b) The normalized first two PCs of winter 200-hPa zonal wind during the period of 1979–2018, derived from EOF analysis. (c–f) Regression of winter zonal wind anomalies (m s^{-1}) at 200 hPa onto the normalized (c, e, g) PC1 and (d, f, h) PC2, derived from (c, b) CRA-40, (e, f) ERA5, and (g, h) CFSR, respectively. In (a, b), the lines indicate the long-term linear trend of the PCs, and *p* and *t* are the probability and trend of lines, respectively. In (c, e, g), the red rectangles outline the key areas of change.

the 200-hPa zonal wind field over Asia for 40 yr (1979–2018) in winter and summer, respectively, the dominant spatial patterns (figures omitted) and PCs (Figs. 7a, b; 9a, b) can be obtained. For convenience, the spatial pattern is represented by the regression of the 200-hPa zonal wind anomalies onto normalized PCs, as illustrated in Figs. 7c–h; 9c–h. Then, the circulations associated with the changes in position and strength of AWJ derived from the three reanalyses are further investigated, as presented in Figs. 8, 10.

In winter, EOF1 is characterized by a tripole distribution, and explains about 33% of the total variance (Figs. 7a, c, e). The two strongest zonal wind anomaly centers appear over East Asia, and two relatively weaker centers reside over West Asia and to the south and north of the jet axis (30°N). EOF2, accounting for 15%–16% of the total variance, is a dipole pattern with relative weaker magnitude than EOF1 (Figs. 7b, d, f). The zonal wind anomalies are located over the western Pacific and Iranian Plateau. In terms of the circulations related to PC1 (Figs. 8a, c, e), East Asia exhibits a dipole pattern with a positive center located over Mongolia and Northeast China and a negative center over South China. Correspondingly, an anomalous anticyclonic–cyclonic circulation is displayed in the meridional direction. On the other hand, West Asia is occupied by negative values accompanied

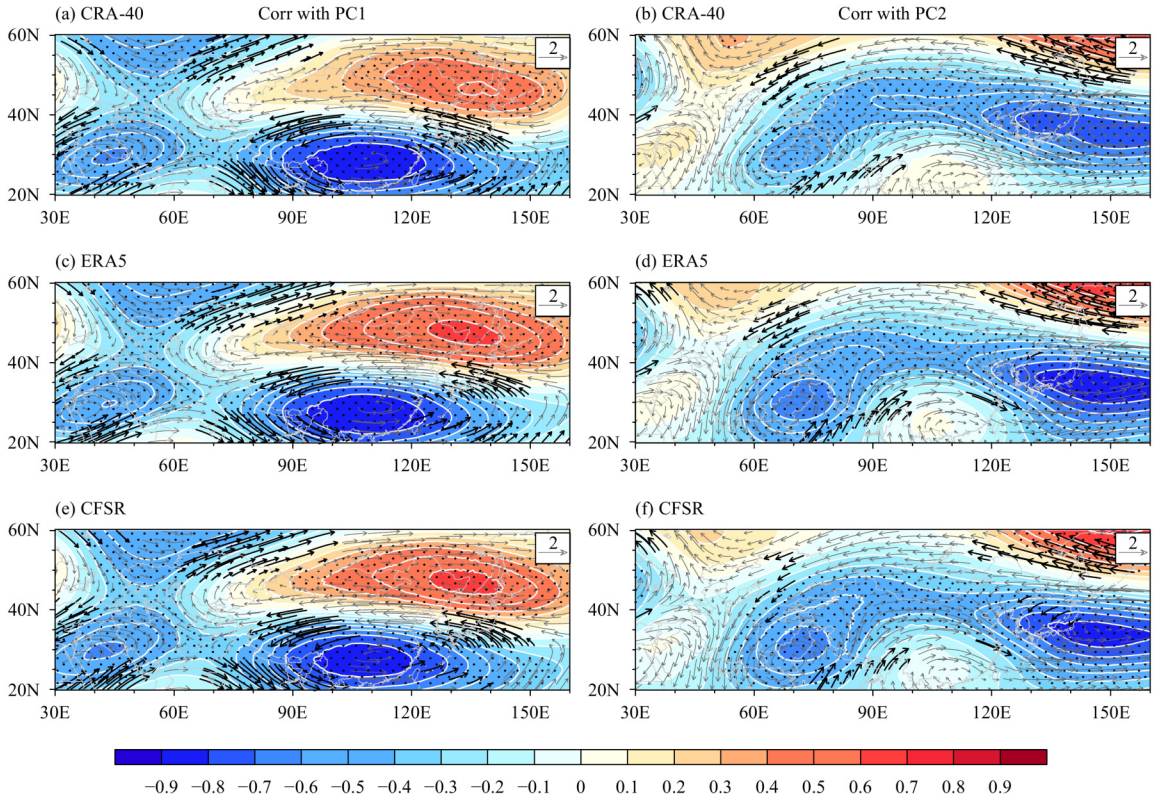

Fig. 8. Circulation anomalies at 200 hPa associated with (a, c, e) PC1 and (b, d, f) PC2 of wintertime AWJ, from (a, b) CRA-40, (c, d) ERA5, and (e, f) CFSR. The vectors denote regressions of 200-hPa winds (m s^{-1}) onto the normalized PCs, and shaded contours denote correlation coefficients between 200-hPa geopotential height and the normalized PCs. PC1 and PC2 are defined as the position and strength indices of the AWJ, respectively. Dots and black vectors denote correlations and regression coefficients significant at the 95% confidence level, respectively.

by anomalous cyclonic circulations. When it turns to PC2 (Figs. 8b, d, f), the majority of Eurasia is occupied by negative correlation coefficients and anomalous cyclonic circulations.

In summer, EOF1 is characterized by a meridional dipole structure with zonal wind anomalies located over Northeast Asia and central Asia, accounting for about 24% of the total variance (Figs. 9a, c, e). EOF2 is dominated by a quarter-pole distribution with negative centers appearing over the Iranian and Mongolian plateaus and positive anomalies over central Asia and East China (Figs. 9b, d, f). Then, the 200-hPa circulations associated with PC1 are given in Figs. 10a, c, e. Significant positive correlations are confined to the middle to high latitudes (30°–50°N). The easterlies prevail over 30°–40°N while the westerlies over the high latitude. In terms of PC2, the 200-hPa circulation anomaly exhibits a Rossby wave anomaly, with anticyclonic circulations over the Mongolian Plateau and cyclonic circulations over central Asia. Eurasia is occupied by a tripole pattern in the zonal direction, with a negative center over central Asia and two positive centers over western Siberia and northern China (Figs. 10b, d, f).

Overall, the EOF decomposition results derived from the three reanalyses are highly consistent with each other in both winter and summer. Furthermore, we calculate statistical results for the EOF reanalysis in four seasons, respectively (figures omitted). The three reanalyses products agree extremely with each other. Differences for variances of EOF1 and EOF2 range almost within 1%. The EOF modes and corresponding PCs are also highly similar to each other, with their correlation coefficients excelling 0.97. In addition, the 200-hPa circulations associated with the changes in position and strength of AWJ derived from the three reanalyses are shown with very tiny discrepancies.

3.4 *Long-term change of AWJ*

In addition to interannual variability, the long-term changes of AWJ are also examined based on the PCs of EOF results. In winter (Figs. 7a, b), PC1s from the three reanalyses all show a statistically significant ($p \leqslant 0.05$) decreasing tendency with a trend of −0.027 during 1979–2018, while no long-term trend is observed in PC2s. In summer (Figs. 9a, b), PC1s decrease slightly (t = −0.012 to −0.021) but are statistically insignificant

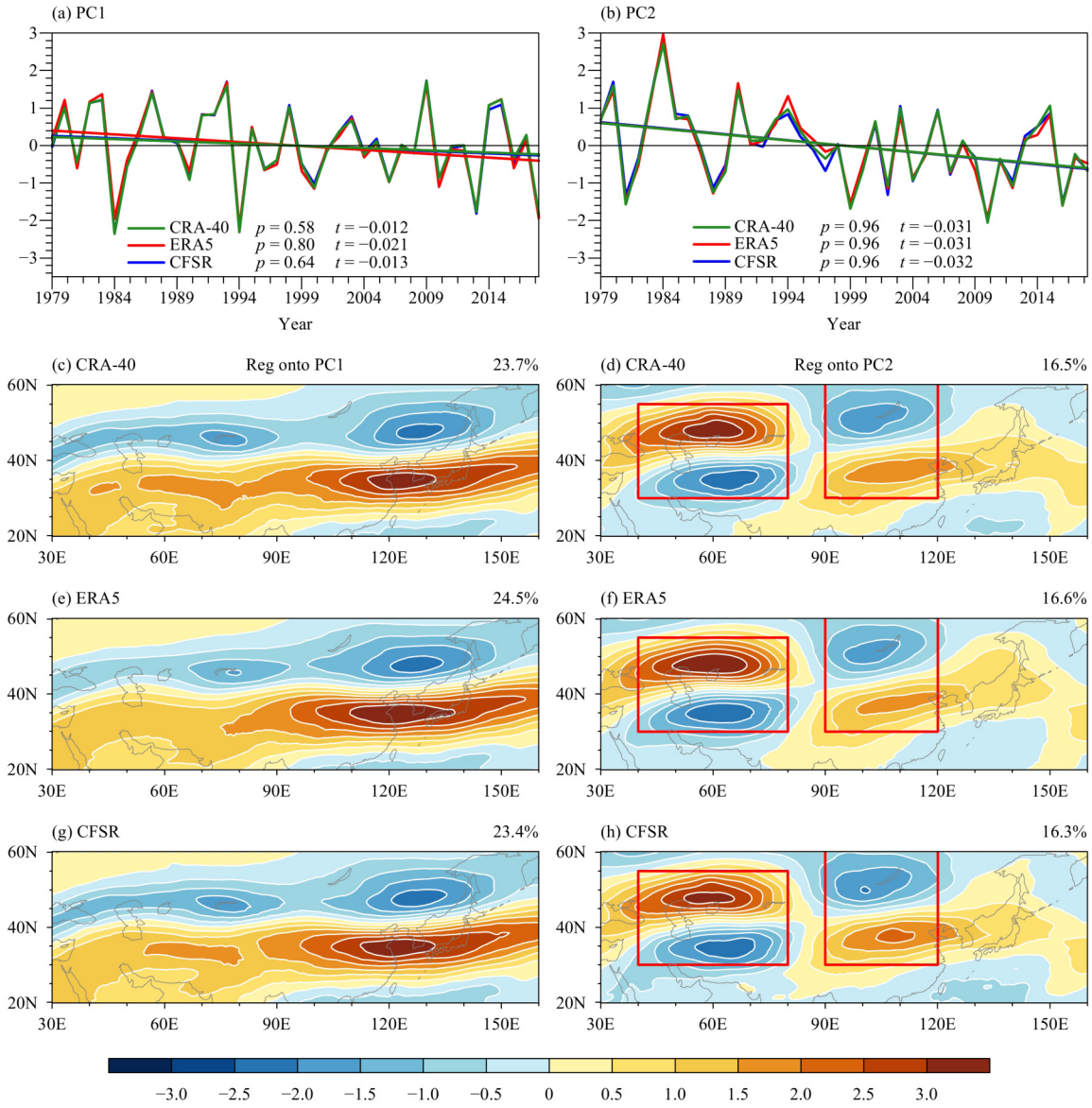

Fig. 9. As in Fig. 7, but for summer.

(p = 0.58–0.80). The PC2s of summertime AWJ from the three reanalyses all show a remarkable decreasing tendency (t = −0.031 to −0.032) statistically significant at the 5% level.

The significant decreasing trends of PC1 in winter and PC2 in summer indicate that the AWJ has changed in the past 40 years. To illustrate the detailed changes of AWJ over the key areas (Figs. 7c, e, g; 9d, f, h), we further show the latitude–time cross-sections of 200-hPa zonal wind anomalies and jet axis from the three reanalyses (Fig. 11). Overall, the evolution in 200-hPa zonal wind anomalies from the three reanalyses resemble each other considerably. Interdedacal changes in the zonal wind anomalies over East Asia are obvious, which occur in the late 1990s in winter (Figs. 11a–c) and the mid 1990s in summer (Figs. 11g–i). In winter, negative anomalies over East Asia are shown to the north of the AWJ axis before the late 1990s, and turns to positive afterwards. In summer, the positive anomalies over East Asia appear before the mid 1990s, and turn to negative afterwards. For the westerly jet over central Asia in summer (Figs. 11d–f), the interdecadal changes are indistinctive.

To further identify the interdecadal changes of the AWJ axis, the 200-hPa mean zonal wind differences between 2000–2018 (1996–2018) and 1979–1999 (1979–1995) in winter (summer) from the three reanalyses are illustrated in Fig. 12. All of the three reanalyses describe considerably consistent distributions of the 200-hPa mean zonal wind differences, which are characterized by a meridional dipole pattern along the jet axis over

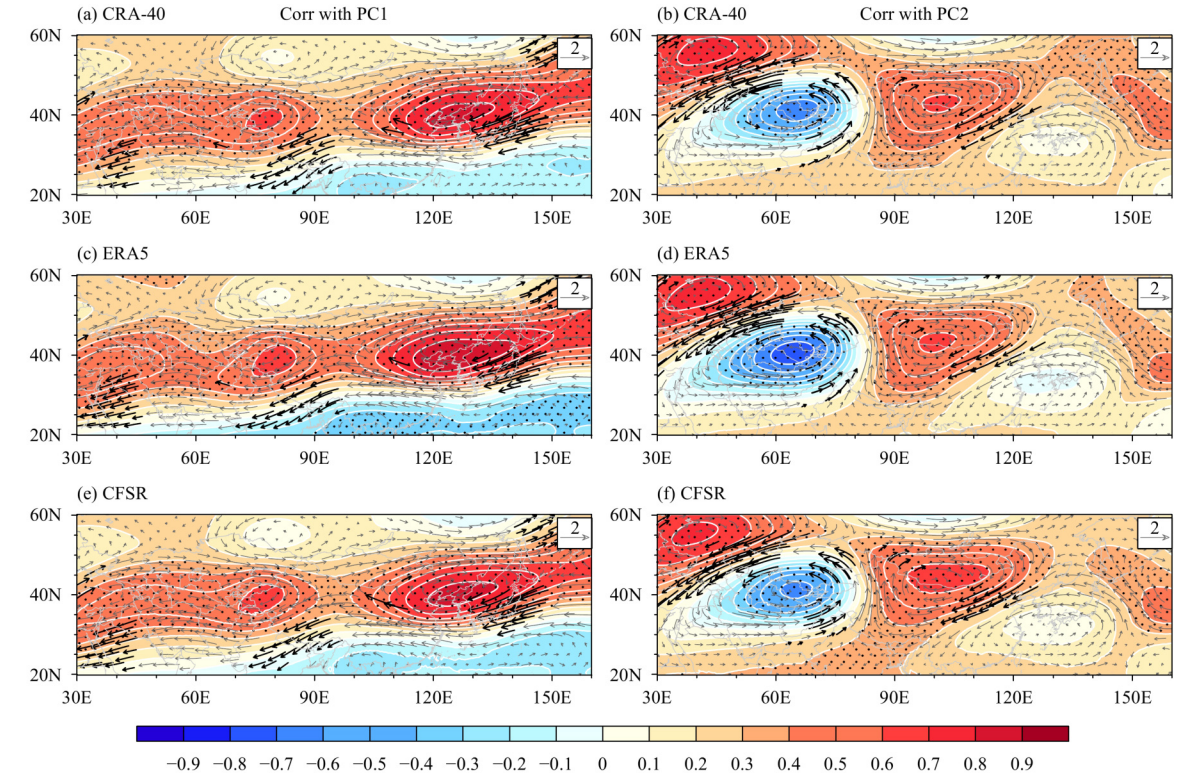

Fig. 10. As in Fig. 8, but for summer.

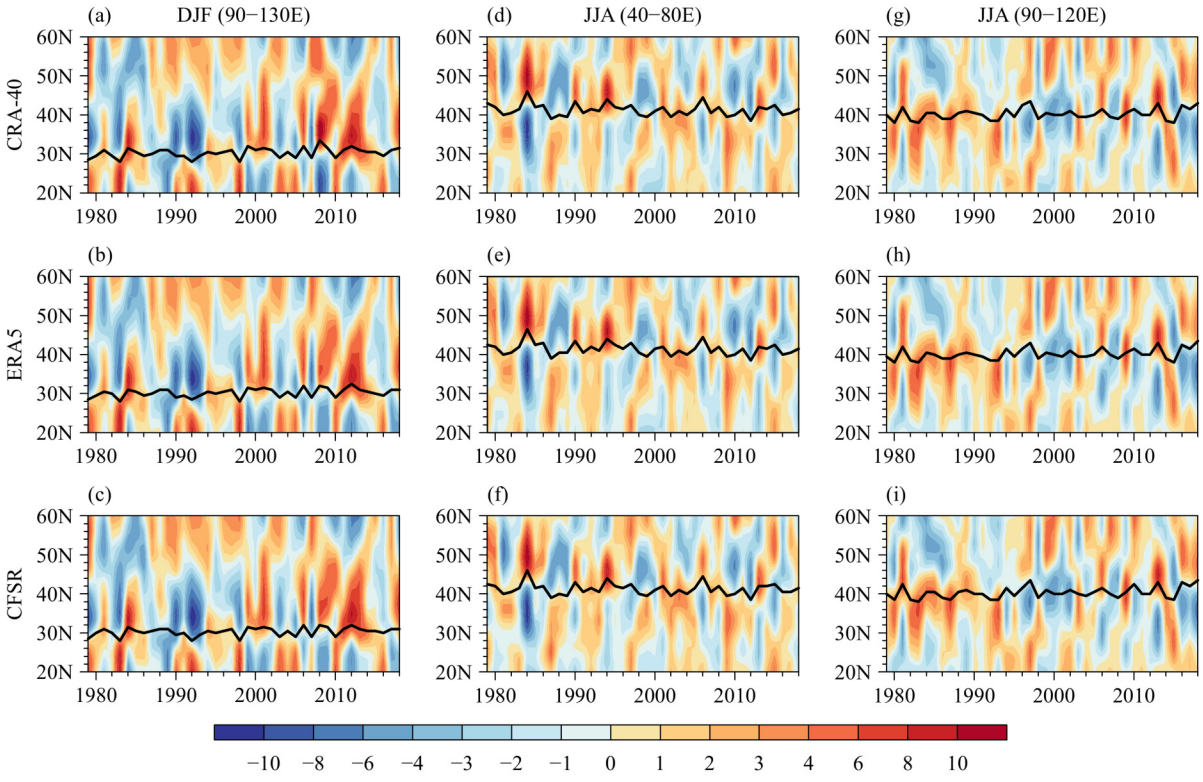

Fig. 11. Latitude–time cross-sections of 200-hPa zonal wind anomalies (m s^{-1}) relative to the mean of 1979–2018, derived from (a, d, g) CRA-40, (b, e, h) ERA5, and (c, f, i) CFSR. The solid lines indicate the locations of AWJ axis. (a–c) East Asian section in winter, averaged along 90°–130°E; (d–f) central Asian section in summer, averaged along 40°–80°E; and (g–i) East Asian section in summer, averaged along 90°–120°E.

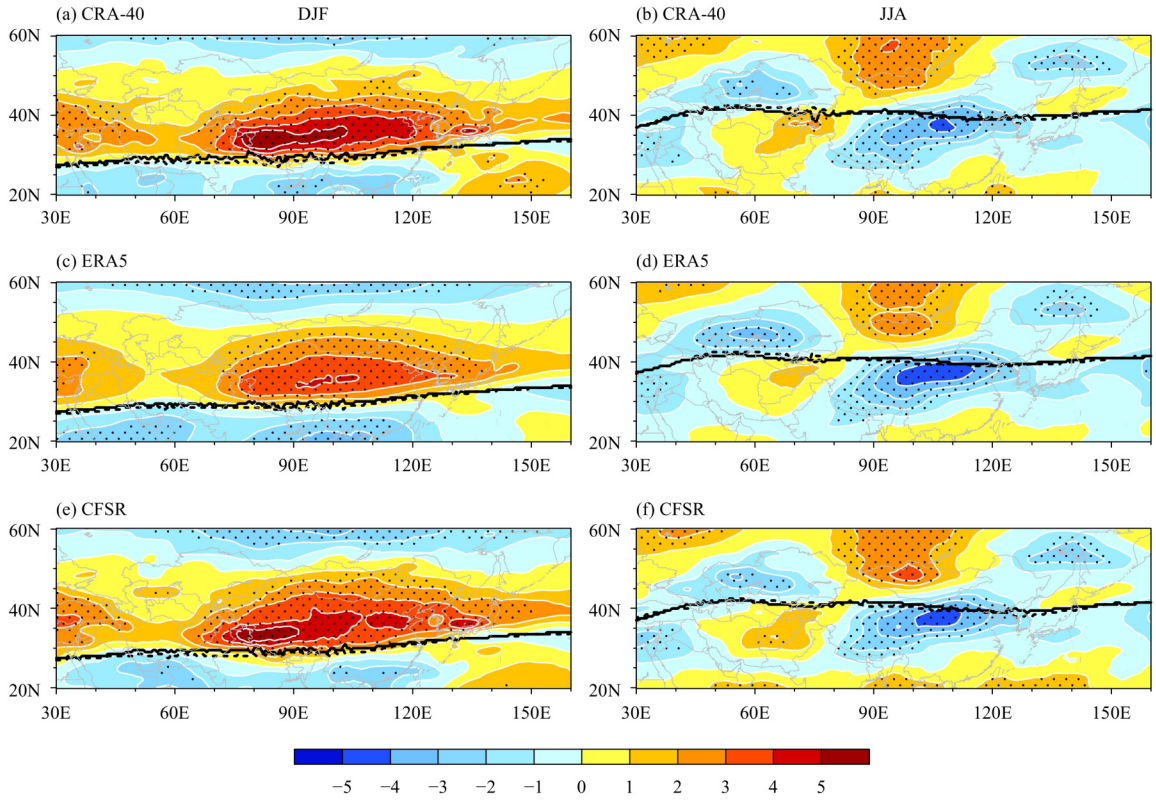

Fig. 12. Decadal changes of 200-hPa zonal winds (m s^{-1}) in winter (2000–2018 minus 1979–1999; left panels) and summer (1996–2018 minus 1979–1995; right panels) from (a, b) CRA-40, (c, d) ERA5, and (e, f) CFSR. The solid and dashed lines indicate the locations of AWJ axis in winter (summer) during 2000–2018 (1996–2018) and 1979–1999 (1979–1995), respectively. Dots represent areas over the 90% confidence level.

East Asia. In winter, the zonal winds enhance to the north of the jet axis while weaken to the south of the jet axis, which means that the wintertime jet axis tends to move northward slightly during the past two decades. In summer, the zonal wind change is characterized by a quarter-pole distribution with positive anomalies over the Iranian and Mongolian plateaus and negative anomalies over East Asia and central Asia. As a result, the jet axis migrates southward over central Asia (40°–80°E) while northward over East Asia (80°–110°E) during the past two decades. Across the three reanalyses, the magnitude of zonal wind enhancement from ERA5 (4 m s^{-1}) is weaker than CRA-40 and CFSR (5 m s^{-1}), especially over the Iranian and Tibetan plateaus regions in winter.

4. Conclusions and discussion

In this study, we made detailed comparison between CRA-40, ERA5, and CFSR during the period of 1979–2018 with respect to the climatic structure, seasonal cycle, interannual variability, and long-term change of AWJ, aiming at evaluating the performance of CMA reanalysis data in describing AWJ. The results are outlined as follows.

(1) The three reanalyses show comparable spatial patterns and quantity both in the horizontal and vertical structures of AWJ, with their pattern correlation coefficients excelling 0.99 and regional average difference values less than 0.4 m s^{-1}. Differences (relative differences) of 200-hPa zonal wind range within ± 0.5 m s^{-1} (± 2%) over a majority of regions, with some distinct differences in winter than in summer. Larger differences with a maximum of ± 2 m s^{-1} (± 5%) appear over the Iranian and Tibetan plateaus regions (50°–90°E) in the mid–upper troposphere in winter.

(2) The three datasets are also highly consistent with each other in the seasonal cycle in terms of the latitude, longitude, and intensity of the AWJ centers (with correlation coefficients ⩾ 0.98). Some obvious discrepancies appear in MAM and SON, especially for the western center (30°–70°E). The correlation coefficients between zonal shift identified in ERA5 and CRA-40 (CFSR) are less than 0.80.

(3) The three reanalyses agree more to each other for the western section than the eastern section in their interannual variability. Among the three metrics (latitude, longitude, and intensity), the three reanalyses present higher consistency in intensity with correlation coeffi-

cient exceeding 0.94 and RMSD $\leqslant$ 2.0 m s^{-1}, but larger differences in longitude with correlation coefficient ranging within 0.8–0.94 and RMSD $\geqslant$ 3 longitudes.

(4) The dominant spatial patterns and corresponding PCs obtained by the EOF decomposition across the three reanalyses strongly resemble each other with their correlation coefficients exceeding 0.97. By defining the PC1 (PC2) as the AWJ position (strength) index, the related circulations at 200 hPa derived from the three reanalyses are shown with some very tiny discrepancies.

(5) The significant decreasing trends of PC1s in winter and PC2s in summer indicate that the AWJ have evident changes during 1979–2018. In winter, the AWJ moves northward with positive zonal wind anomaly over most parts of China. In summer, the westerly jet undergoes a southward displacement over central Asia (40°–80°E) and a northward migration over East Asia (80°–110°E). It is noticeable that the magnitude of zonal wind enhancement to the north of the AWJ axis is weaker from ERA5 than from CRA-40 and CFSR, especially over the Iranian and Tibetan plateaus in winter.

This study has systematically verified the considerable agreement among the three reanalyses on the above perspectives. Extended discussion is as follows. 1) Due to more observations over East Asia that have been assimilated in the CRA system (Liao et al., 2018; Wang et al., 2018; Yin et al., 2018), it is presumable that CRA-40 is more reliable in depicting the atmospheric circulations over East Asia. Nonetheless, some discrepancies in describing the characteristics of EAWJ and its associated atmospheric circulations across the three reanalyses indeed exist. 2) In terms of absolute values, the biggest differences across the three reanalyses appear in winter, which is mainly because AWJ is much stronger in winter than in summer. 3) Regionally, the biggest differences across the three reanalyses lie in the Iranian and Tibetan plateaus. This may be attributable to the complex topography, which has evident dynamic and thermal effects on the troposphere (Yeh, 1982; Xia et al., 2016; Jiang et al., 2020) and depends highly on models (Gao et al., 2017; Li et al., 2018) and data assimilation (Seto et al., 2013; Yu et al., 2018; He et al., 2019). In summary, this study has demonstrated the rationality and reliability of CRA-40 in characterizing the AWJ, and provided support to use of CRA-40 in analyzing the large-scale atmospheric circulations in East Asia in future.

REFERENCES

Dao, S. Y., Y. J. Zhao, and X. M. Chen, 1958: The relationship between May-Yü in Far East and the behaviour of circulation over Asia. *Acta Meteor. Sinica*, **29**, 119–134, doi: 10.11676/qxxb1958.014. (in Chinese)

Dao, S. Y., Y. F. Li, and Y. P. Wen, 1965: A preliminary study on the general circulation of East Asia in the upper troposphere and stratosphere. *Acta Meteor. Sinica*, **35**, 155–165, doi: 10.11676/qxxb1965.019. (in Chinese)

Dee, D. P., S. M. Uppala, A. J. Simmons, et al., 2011: The ERA-Interim reanalysis: configuration and performance of the data assimilation system. *Quart. J. Roy. Meteor. Soc.*, **137**, 553–597, doi: 10.1002/qj.828.

Du, Y., Q. Bao, and Z. Q. Xie, 2017: FGOALS model simulation of variation of East Asian subtropical westerly jet during Meiyu period. *Chinese J. Atmos. Sci.*, **41**, 603–617, doi: 10.3878/j.issn.1006-9895.1609.16185. (in Chinese)

Du, Y., Y. C. Zhang, and Z. Q. Xie, 2009: Location variation of the East Asia subtropical westerly jet and its effect on the summer precipitation anomaly over eastern China. *Chinese J. Atmos. Sci.*, **33**, 581–592, doi: 10.3878/j.issn.1006-9895.2009.03.15. (in Chinese)

Du, Y., T. Li, Z. Q. Xie, et al., 2016: Interannual variability of the Asian subtropical westerly jet in boreal summer and associated with circulation and SST anomalies. *Climate Dyn.*, **46**, 2673–2688, doi: 10.1007/s00382-015-2723-x.

Fu, Y. H., Z. D. Lin, and D. Guo, 2020: Improvement of the simulation of the summer East Asian westerly jet from CMIP5 to CMIP6. *Atmos. Ocean. Sci. Lett.*, **13**, 550–558, doi: 10.1080/16742834.2020.1746175.

Gao, Y. H., L. H. Xiao, D. L. Chen, et al., 2017: Quantification of the relative role of land-surface processes and large-scale forcing in dynamic downscaling over the Tibetan Plateau. *Climate Dyn.*, **48**, 1705–1721, doi: 10.1007/s00382-016-3168-6.

Gibson, J. K., P. W. Kållberg, S. Uppala, et al., 1997: ERA Description. ECMWF, Shinfield Park, Reading, 89 pp.

He, J., F. Q. Zhang, X. C. Chen, et al., 2019: Development and evaluation of an ensemble-based data assimilation system for regional reanalysis over the Tibetan Plateau and surrounding regions. *J. Adv. Model. Earth Syst.*, **11**, 2503–2522, doi: 10.1029/2019MS001665.

Hersbach, H., and D. Dee, 2016: ERA5 reanalysis is in production. *ECMWF Newsletter*, **147**, 7–7. Available online at https://www.ecmwf.int/en/newsletter/147/news/era5-reanalysis-production. Accessed on 12 January 2021.

Huang, A. N., Y. Zhou, Y. C. Zhang, et al., 2014: Changes of the annual precipitation over central Asia in the twenty-first century projected by multimodels of CMIP5. *J. Climate*, **27**, 6627–6646, doi: 10.1175/JCLI-D-14-00070.1.

Huang, G., and Y. Liu, 2011: Simulation of the East Asian subtropical westerly jet stream with GFDL AGCM (AM2.1). *Atmos. Ocean. Sci. Lett.*, **4**, 24–29, doi: 10.1080/16742834.2011.11446902.

Huang, W., S. Feng, J. H. Chen, et al., 2015: Physical mechanisms of summer precipitation variations in the Tarim basin in northwestern China. *J. Climate*, **28**, 3579–3591, doi: 10.1175/JCLI-D-14-00395.1.

Hunt, K. M. R., J. Curio, A. G. Turner, et al., 2018: Subtropical westerly jet influence on occurrence of western disturbances and Tibetan Plateau vortices. *Geophys. Res. Lett.*, **45**, 8629–8636, doi: 10.1029/2018GL077734.

Ji, K., S. X. Wang, H. C. Zuo, et al., 2020: Effect of meridional

position of East Asian subtropical jet on midsummer precipitation in eastern part of Northwest China. *Arid Zone Res.*, **37**, 10–17, doi: 10.13866/j.azr.2020.01.02. (in Chinese)

Jiang, Y. S., F. Chen, Y. H. Gao, et al., 2020: Assessment of uncertainty sources in snow cover simulation in the Tibetan Plateau. *J. Geophs. Res. Atmos.*, **125**, e2020JD032674, doi: 10.1029/2020JD032674.

Kuang, X. Y., Y. C. Zhang, and J. Liu, 2007: Seasonal variation of the East Asian subtropical westerly jet and its thermal mechanism. *Acta Meteor. Sinica*, **21**, 192–203.

Li, C., and J. L. Sun, 2015: Role of the subtropical westerly jet waveguide in a southern China heavy rainstorm in December 2013. *Adv. Atmos. Sci.*, **32**, 601–612, doi: 10.1007/s00376-014-4099-y.

Li, C. X., T. B. Zhao, C. X. Shi, et al., 2020: Evaluation of daily precipitation product in China from the CMA global atmospheric interim reanalysis. *J. Meteor. Res.*, **34**, 117–136, doi: 10.1007/s13351-020-8196-9.

Li, X., Y. H. Gao, Y. J. Pan, et al., 2018: Evaluation of near-surface wind speed simulations over the Tibetan Plateau from three dynamical downscalings based on WRF model. *Theor. Appl. Climatol.*, **134**, 1399–1411, doi: 10.1007/s00704-017-2353-9.

Liang, X., L. P. Jiang, Y. Pan, et al., 2020: A 10-yr global land surface reanalysis interim dataset (CRA-Interim/Land): Implementation and preliminary evaluation. *J. Meteor. Res.*, **34**, 101–116, doi: 10.1007/s13351-020-9083-0.

Liao, J., K. X. Hu, H. Jiang, et al., 2018: Pre-process and data selection for assimilation of conventional observations in the CMA global atmospheric reanalysis. *Adv. Meteor. Sci. Technol.*, **8**, 133–142, doi: 10.3969/j.issn.2095-1973.2018.01.018. (in Chinese)

Liao, Q. H., S. Y. Tao, and H. J. Wang, 2004: Interannual variation of summer subtropical westerly jet in East Asia and its impacts on the climate anomalies of East Asia summer monsoon. *Chinese J. Geophys.*, **47**, 12–21, doi: 10.1002/cjg2.449.

Lin, Z. D., and R. Y. Lu, 2005: Interannual meridional displacement of the East Asian upper-tropospheric jet stream in summer. *Adv. Atmos. Sci.*, **22**, 199–211, doi: 10.1007/BF02918509.

Lin, Z. D., Y. H. Fu, and R. Y. Lu, 2019: Intermodel diversity in the zonal location of the climatological East Asian westerly jet core in summer and association with rainfall over East Asia in CMIP5 models. *Adv. Atmos. Sci.*, **36**, 614–622, doi: 10.1007/s00376-019-8221-z.

Liu, Z. Q., C. X. Shi, Z. J. Zhou, et al., 2017: CMA global reanalysis (CRA-40): Status and plans. Proc. 5th International Conference on Reanalysis, 13–17 November, Nat. Meteor. Int. Canter, Rome, Italy, 1–16.

Lu, J. H., and T. Schneider, 2017: Evolving perspectives on abrupt seasonal changes of the general circulation. *Adv. Atmos. Sci.*, **34**, 1185–1194, doi: 10.1007/s00376-017-7068-4.

Peng, D. D., and T. J. Zhou, 2017: Why was the arid and semiarid northwest China getting wetter in the recent decades? *J. Geophys. Res. Atmos.*, **122**, 9060–9075, doi: 10.1002/2016JD026424.

Saha, S., S. Moorthi, H. L. Pan, et al., 2010: The NCEP climate forecast system reanalysis. *Bull. Amer. Meteor. Soc.*, **91**, 1015–1058, doi: 10.1175/2010BAMS3001.1.

Saha, S., S. Moorthi, X. R. Wu, et al., 2014: The NCEP Climate Forecast System version 2. *J. Climate*, **27**, 2185–2208, doi: 10.1175/JCLI-D-12-00823.1.

Schiemann, R., D. Lüthi, and C. Schär, 2009: Seasonality and interannual variability of the westerly jet in the Tibetan Plateau region. *J. Climate*, **22**, 2940–2957, doi: 10.1175/2008JCLI2625.1.

Seto, R., T. Koike, and M. Rasmy, 2013: Analysis of the vertical structure of the atmospheric heating process and its seasonal variation over the Tibetan Plateau using a land data assimilation system. *J. Geophs. Res. Atmos.*, **118**, 12403–12421, doi: 10.1002/2013JD020072.

Staff Members of the Section of Synoptic and Dynamic Meteorology, Institute of Geophysics and Meteorology, Academia Sinica, 1957: On the general circulation over Eastern Asia (I). *Tellus*, **9**, 432–446, doi: 10.3402/tellusa.v9i4.9136.

Staff Members of the Section of Synoptic and Dynamic Meteorology, Institute of Geophysics and Meteorology, Academia Sinica, 1958a: On the general circulation over Eastern Asia (II). *Tellus*, **10**, 58–75, doi: 10.3402/tellusa.v10i1.9219.

Staff Members of the Section of Synoptic and Dynamic Meteorology, Institute of Geophysics and Meteorology, Academia Sinica, 1958b: On the general circulation over Eastern Asia (III). *Tellus*, **10**, 299–312, doi: 10.3402/tellusa.v10i3.9250.

Uppala, S. M., P. W. KÅllberg, A. J. Simmons, et al., 2005: The ERA-40 reanalysis. *Quart. J. Roy. Meteor. Soc.*, **131**, 2961–3012, doi: 10.1256/qj.04.176.

Wang, M. Y., S. Yao, L. P. Jiang, et al., 2018: Collection and preprocessing of satellite remote-sensing data in CRA-40 (CMA's global atmospheric reanalysis). *Adv. Meteor. Sci. Technol.*, **8**, 158–163, doi: 10.3969/j.issn.2095-1973.2018.01.021. (in Chinese)

Wei, W., R. H. Zhang, M. Wen, et al., 2017: Relationship between the Asian westerly jet stream and summer rainfall over central Asia and north China: Roles of the Indian monsoon and the South Asian high. *J. Climate*, **30**, 537–552, doi: 10.1175/JCLI-D-15-0814.1.

Xia, X., R. C. Ren, G. X. Wu, et al., 2016: An analysis on the spatiotemporal variations and dynamic effects of the tropopause and the related stratosphere–troposphere coupling surrounding the Tibetan Plateau area. *Acta Meteor. Sinica*, **74**, 525–541, doi: 10.11676/qxxb2016.036. (in Chinese)

Xie, Z. Q., Y. Du, and S. Yang, 2015: Zonal extension and retraction of the subtropical westerly jet stream and evolution of precipitation over East Asia and the western Pacific. *J. Climate*, **28**, 6783–6798, doi: 10.1175/JCLI-D-14-00649.1.

Yan, Y. H., C. F. Li, and R. Y. Lu, 2019: Meridional displacement of the East Asian upper-tropospheric westerly jet and its relationship with the East Asian summer rainfall in CMIP5 simulations. *Adv. Atmos. Sci.*, **36**, 1203–1216, doi: 10.1007/s00376-019-9066-1.

Yan, Z. B., Z. H. Lin, and H. Zhang, 2014: The relationship between the East Asian subtropical westerly jet and summer precipitation over East Asia as simulated by the IAP AGCM4.0. *Atmos. Ocean. Sci. Lett.*, **7**, 487–492, doi: 10.3878/AOSL20140048.

Yang, L. M., and Q. Y. Zhang, 2008a: Climate features of summer Asia subtropical westerly jet stream. *Climatic Environ. Res.*, **13**, 10–20. (in Chinese)

Yang, L. M., and Q. Y. Zhang, 2008b: Interannual variation of summer precipitation in Xinjiang and Asian subtropical westerly jet stream. *J. Appl. Meteor. Sci.*, **19**, 171–179, doi: 10.3969/j.issn.1001-7313.2008.02.006. (in Chinese)

Yeh, T. C., 1982: Some aspects of the thermal influences of the Qinghai–Tibetan Plateau on the atmospheric circulation. *Arch. Met. Geoph. Biocl. A.*, **31**, 205–220, doi: 10.1007/BF02258032.

Yeh, T. C., S. Y. Dao, and M. T. Li, 1958: The abrupt change of circulation over Northern Hemisphere during June and October. *Acta Meteor. Sinica*, **29**, 249–263. (in Chinese)

Yin, J. F., X. D. Liang, F. Chen, et al., 2018: Development of atmospheric data assimilation techniques and regional reanalysis datasets in the East Asia. *Adv. Meteor. Sci. Techol.*, **8**, 79–84, doi: 10.3969/j.issn.2095-1973.2018.01.009. (in Chinese)

Yu, X. J., J. Du, M. Z. Wang, et al., 2018: Impact of assimilating the new radiosonde data over Qinghai–Tibetan Plateau on summer rainfall forecast over southern Xinjiang. *Plateau Meteor.*, **37**, 13–27, doi: 10.7522/j.issn.1000-0534.2017.00034. (in Chinese)

Zhang, Y. C., and D. Q. Huang, 2011: Has the East Asian westerly jet experienced a poleward displacement in recent decades? *Adv. Atmos. Sci.*, **28**, 1259–1265, doi: 10.1007/s00376-011-9185-9.

Zhang, Y. C., X. Y. Kuang, W. D. Guo, et al., 2006: Seasonal evolution of the upper-tropospheric westerly jet core over East Asia. *Geophys. Res. Lett.*, **33**, L11708, doi: 10.1029/2006GL026377.

Zhao, B., B. Zhang, C. X. Shi, et al., 2019: Comparison of the global energy cycle between Chinese reanalysis interim and ECMWF reanalysis. *J. Meteor. Res.*, **33**, 563–575, doi: 10.1007/s13351-019-8129-7.

Zhao, Y., M. Z. Wang, A. N. Huang, et al., 2014a: Relationships between the West Asian subtropical westerly jet and summer precipitation in northern Xinjiang. *Theor. Appl. Climatol.*, **116**, 403–411, doi: 10.1007/s00704-013-0948-3.

Zhao, Y., A. N. Huang, Y. Zhou, et al., 2014b: Impact of the middle and upper tropospheric cooling over central Asia on the summer rainfall in the Tarim Basin, China. *J. Climate*, **27**, 4721–4732, doi: 10.1175/JCLI-D-13-00456.1.

Zhao, Y., X. J. Yu, J. Q. Yao, et al., 2018: Evaluation of the subtropical westerly jet and its effects on the projected summer rainfall over central Asia using multi-CMIP5 models. *Int. J. Climatol.*, **38**, e1176–e1189, doi: 10.1002/joc.5443.

Zhao, Y., X. J. Yu, J. Q. Yao, et al., 2019: The concurrent effects of the South Asian monsoon and the plateau monsoon over the Tibetan Plateau on summer rainfall in the Tarim Basin of China. *Int. J. Climatol.*, **39**, 74–88, doi: 10.1002/joc.5783.

Zhu, B. Z., Y. H. Ding, and H. B. Luo, 1990: A review of the atmospheric general circulation and monsoon in East Asia. *Acta Meteor. Sinica*, **4**, 399–416.

Tech & Copy Editor: Lan YI